Sustainable Energy, Grids and Networks 2 (2015) 69–82

Contents lists available at ScienceDirect

Sustainable Energy, Grids and Networks

journal homepage: www.elsevier.com/locate/segan

A PMU-based state estimator considering classic HVDC links under different control modes

Wei Li [a,*], Luigi Vanfretti [a,b]

[a] KTH Royal Institute of Technology, School of Electrical Engineering, Electric Power Systems, Teknikringen 33, SE-100 44 Stockholm, Sweden
[b] Statnett SF, Research & Development, Nydalen Allé 33, 0423 Oslo, Norway

ARTICLE INFO

Article history:
Received 18 September 2014
Received in revised form
6 March 2015
Accepted 28 April 2015
Available online 9 May 2015

Keywords:
PMU-based state estimation
Classic HVDC link
PMU
Hybrid AC and DC state estimation

ABSTRACT

This paper aims to develop a PMU-based state estimation algorithm that considers the presence of classic HVDC links operating under different control modes. Thus, hybrid AC/DC grid state estimation becomes feasible. In this algorithm we assume that DC link measurements can be sampled and reported at the same rate as PMU measurements, so that both AC and DC states can be estimated simultaneously in real-time. The estimation algorithm uses synchrophasors in polar coordinates, which allows angle bias detection and correction. In addition, some practical issues for the proposed state estimator are discussed, including observability and measurement redundancy, measurement noise and weightings, and angle bias correction. Finally, study cases using different power system models are carried out to show the state estimator's performances during both steady conditions and dynamic changes. Relatively small residuals during steady conditions validate accuracy; results during dynamic changes verify the estimator's reliability.

1. Introduction

Power system state estimation (SE) is a process used to determine the state of a network by using measurements and a model of the grid. With a proper redundancy level, SE can eliminate the effect of bad data and produce reliable state estimates in order to help operators monitor the grid and to support other analysis functions in energy management systems (EMS) [1].

1.1. A PMU-based state estimator

Conventional SE [1,2] uses a combination of measurements provided by traditional supervisory control and data acquisition (SCADA) systems and pseudo-measurements. At the same time, some of these measurements are state variables to be estimated. These measurements are asynchronous and provided every two to ten seconds, which limits the speed at which the state estimator can be executed, regardless of the speed of the numerical algorithm used for estimation. The network model for conventional SE, by its nature, contains numerous nonlinearities in contrast with circuit analysis models [3].

With the remarkable growth of synchronized phasor measurement units (PMUs) installations in power systems, new types of SE methods based on synchrophasor measurements have been proposed and tested, for instance, [4–6]. With respect to measurements, PMUs provide GPS time-synchronized measurements at a rate of 30–50 samples per second to PMU-based state estimators. Compared to that in SCADA systems (measurement every two to ten seconds per sample), this rate enables static SE to follow the states' trajectories. On the other hand, such synchronous data rate requires a numerical algorithm for estimation that (i) can be executed faster than the PMU reporting rate, and (ii) offers a sufficiently simple mathematical representation of the grid to allow fast updates when changes occur in the power system, without sacrificing accuracy. Having such numerical algorithm available, a PMU-based state estimator could help in sanitizing synchrophasor data and supporting other PMU applications. Moreover, various PMU applications [7] can also benefit from a PMU-based state estimation (PSE).

Another difference is that PMU measurement quantities are voltage and current phasors, which are state variables at the same time. This characteristic significantly decreases the dimension of the SE network model compared to that of the conventional SE, and can lead to a mathematical representation with far less nonlinearities as long as circuit analysis models are applied instead of power flow models. This kind of simple representation will in turn mitigate numerical computation burden.

* Corresponding author.
E-mail address: wei3@kth.se (W. Li).

http://dx.doi.org/10.1016/j.segan.2015.04.004
2352-4677/

Today, PMUs are not as ubiquitous as SCADA measurements, and thus they are regarded as a complement to SCADA measurements in conventional SE. [8] presents an approach to incorporate the PMU measurements within a conventional SE assuming that the conventional SE must function normally in the absence of PMU data. [9] introduces a multistage SE that separates phasor measurements from a SCADA-based estimator and processes them distinctly. In [10], a whole power system is decoupled into PMU- and SCADA-observed areas and the estimation is computed sequentially. This approach greatly relies on system measurement configuration and topology connectivity. Similarly to these three articles, most related publications aim to preserve the mathematical representations of the conventional SEs, avoiding changes to it as much as possible. In a sense, in these approaches, PMUs become common metering devices, not differing much with others. However, this comes at the cost of not exploiting the advantages of PMU measurements, which are fast reporting rate and time synchronization.

Mixing PMU measurements with SCADA measurements for conventional SE is only a temporary solution when considering an insufficient number of PMUs in a system. However, it is foreseen that in the near future PMUs could cover most areas of power systems at least at high-voltage substations. PMUs will thus become omnipresent metering devices, in the same way that SCADA metering devices are now.

Based on the above considerations, this paper proposes a PMU-only SE algorithm, in which Kirchhoff's laws are applied with voltage and current phasors exclusively, significantly reducing the nonlinearities of the network model and the computation burden of the numerical solution algorithm. In addition, magnitudes and angles of the PMU measurements are uncorrelated in polar coordinates, which is greatly different from the linear state estimator presented in [11] where the phasors are used in rectangular coordinates. Thus, analyzing magnitude and angle data independently allows angle bias detection and correction [4–6], which will be also addressed in this paper.

1.2. Modeling of classic HVDC links under different control modes

Power electronic-based devices are becoming more common in power systems, and there are several papers considering FACTS devices in state estimation [12,13]. However, to the best knowledge of the authors, previously work has not fully considered hybrid AC/DC grids. Classic HVDC technology is mature and has been used worldwide. It is still irreplaceable for HVDC applications of high power and voltage ratings, which can be up to 8000 MW, with voltages up to 800 kV [14]. Although classic HVDC links have been included in conventional SE network models [15,16], the use of conventional measurements makes the SE model complex. Therefore, the main contribution of this paper is to include classic high voltage direct current (HVDC) links into the PSE network model.

The fast sampling rate of PMUs in the AC grid can assist system operators to track fast DC control, which cannot be supported by the slow-rate measurements in SCADA systems. The proposed PSE algorithm in this paper takes classic HVDC links into consideration so that a PSE for hybrid AC/DC grids becomes feasible. It uses PMU measurements from the AC network, and assumes that measurements of the DC link are sampled synchronously and time-stamped by GPS at the same rate as PMU data.

Paper [11] proposes a linear classic HVDC link model for PSE, however, it is simplified and has not considered different control modes. To the authors' knowledge, none of the published SE models consider the control modes of the HVDC link, which in fact could bring benefits to the performance and accuracy of state estimators. This will be illustrated by a comparison between the linear DC link model in [11] and the nonlinear one proposed in this paper. Moreover, as classic HVDC control technology is mature and robust, the controlled states can be steadily maintained at their references, which can be provided as an input to the PSE model. Hence, applying the corresponding references into the network model will provide additional robustness to the PSE.

When the PSE is applied to hybrid AC/DC grids, all the related issues for AC state estimators, such as system observability and measurements redundancy, measurement noises and weightings, and bad data detection and correction, have to be addressed. In particular, this paper provides new rules for observability analysis when considering HVDC links for PSE. Solutions for such issues are devised in this paper by taking advantage of phasor measurements.

1.3. Article organization

This paper is organized as follows. Section 2 describes the PSE algorithm. In Section 3, network models of a unified AC network branch model, a classic HVDC link, and their interface are introduced. Then the PSE for a hybrid AC/DC grid is presented in Section 4. Section 5 discusses the PSE practical application issues, including system observability and measurement redundancy, measurement noise and weighting's selection, and angle bias correction. Then the PSE algorithm is validated through simulations of two different test systems in Section 6. Finally, Section 7 discusses the differences between the linear state estimator in previous work [11] and the nonlinear one presented in this paper in order to highlight the advantages of using the nonlinear PSE.

2. PMU-based state estimation algorithm

The conventional SE formulation for nonlinear systems is based on the nonlinear measurement model [1]:

$$\mathbf{z} = \mathbf{h}(\mathbf{x}) + \mathbf{e}, \tag{1}$$

where $\mathbf{z} \in \mathbb{R}^m$ is the measurement vector, $\mathbf{x} \in \mathbb{R}^n$ is the state vector, $\mathbf{h} : \mathbb{R}^n \rightarrow \mathbb{R}^m$ is a nonlinear function relating measurements to states, and $\mathbf{e} \in \mathbb{R}^m$ is the measurement error vector, which is assumed to have a normal distribution, i.e., $\mathbf{e} \sim \mathcal{N}(0, \mathbf{R_z})$. $\mathbf{R_z}$ denotes the corresponding measurement covariance matrix.

The measurement variables of a conventional state estimator include flow measurements, e.g. active power flow measurements (P_{ft}^{meas}), reactive power flow measurements (Q_{ft}^{meas}), current magnitude measurements ($|I_{ft}^{meas}|$); and bus injection measurements, e.g. active power injection measurements (P_i^{meas}), reactive power injection measurements (Q_i^{meas}), injected current magnitude measurements ($|I_i^{meas}|$). On the other hand, state variables are mainly bus voltage magnitudes and angles. Therefore, measurement variables and states are explicitly separated, as expressed in (1).

However, when PMUs are used for data acquisition, the state variables can be measured directly, that is $\widetilde{\mathbf{V}}$, $\widetilde{\mathbf{I}}$ phasors. A direct consequence is that the choice of state variables $\mathbf{x}$ to be measurement variables $\mathbf{z}$ in (1) cannot be uniquely determined. Therefore, the choice will affect estimation accuracy of different states. Any variable chosen to be $\mathbf{z}$ in the measurement model will lose the corresponding element in the Jacobian matrix. In other words, the network model and corresponding Jacobian matrix are not unique. Based on above consideration, a new measurement model is needed to separate the measurement variables from the network model. The proposed measurement model is formulated as follows:

$$\mathbf{e} = \begin{bmatrix} \mathbf{h}(\mathbf{x}) \\ \mathbf{x} \end{bmatrix} - \begin{bmatrix} \mathbf{0} \\ \mathbf{z} \end{bmatrix}, \tag{2}$$

where $\mathbf{h} : \mathbb{R}^n \rightarrow \mathbb{R}^k$, k is the number of network model equations.

If a power system has more measurements than states, i.e. $m > n$, the state estimator will conduct the weighted least squares (WLS) algorithm to solve an over-determined problem. The performance index $J(\mathbf{x})$ based on the proposed measurement model is expressed as follows:

$$J(\mathbf{x}) = \frac{1}{2}\left[\sum_{i=1}^{k}\left(\frac{h_i(\hat{\mathbf{x}})}{\sigma_i}\right)^2 + \sum_{j=1}^{m}\left(\frac{\hat{x}_j - z_j}{\sigma_j}\right)^2\right], \tag{3}$$

where the inverse of σ_i^2 is the weighting of the ith network equation in the WLS, the inverse of σ_j^2 is the weighting of the jth measurement. In order to minimize the estimation error, the performance index $J(\mathbf{x})$ should be minimized. This can be achieved when σ_i equals to the standard variance of the ith network model equation error and σ_j equals to the standard variance of the jth measurement.

Numerical methods for solving non-linear algebraic equations (e.g. Gauss–Newton and Newton–Raphson methods) can be used to solve the nonlinear WLS problem, which have been described in the literature, e.g., [1,2]. Thereby, we apply a commonly used iteration procedure to obtain the updated state $\hat{\mathbf{x}}$, as follows:

$$\begin{aligned}(\mathbf{H}^T(\hat{\mathbf{x}}^i)\mathbf{R}^{-1}\mathbf{H}(\hat{\mathbf{x}}^i))^{-1}\Delta\hat{\mathbf{x}}^i &= \mathbf{H}^T(\hat{\mathbf{x}}^i)\mathbf{R}^{-1}\Delta\mathbf{z}(\hat{\mathbf{x}}^i),\\ \hat{\mathbf{x}}^{i+1} &= \hat{\mathbf{x}}^i + \Delta\hat{\mathbf{x}}^i,\end{aligned} \tag{4}$$

where

$$\Delta\mathbf{z}(\hat{\mathbf{x}}^i) = \begin{bmatrix}\mathbf{h}(\hat{\mathbf{x}}^i)\\ \hat{\mathbf{x}}^i - \mathbf{z}\end{bmatrix},$$

$\mathbf{H}(\mathbf{x})$ is the Jacobian matrix of the first order derivative of $J(\mathbf{x})$, and $\mathbf{R}$ denotes the covariance matrix with σ_i^2 and σ_j^2 on its diagonal.

Note that this measurement model and its Jacobian matrix have higher dimensions compared to those in the conventional state estimator. However, it does not result in much computational burden since the elements in both of them are very simple, the former is the differences between state variables and measurements $[\mathbf{x} - \mathbf{z}]$ and the latter is an identify matrix.

3. Hybrid AC/DC network model

A state estimator determines the real-time condition of a network by using dynamic data (PMU measurements) and static network data (connectivity configuration and model parameters). Thus, building a static network model is a crucial step. Note that in this paper, it is assumed that the network topology remains the same, thus the static network model does not need to consider the statues of switching devices, a task that is more relevant for a topology processor [1,2].

PMUs measure voltage phasors $\tilde{\mathbf{V}}$ at the buses where PMUs are installed and current phasors $\tilde{\mathbf{I}}$ on the lines adjacent to the buses. Directly using $\tilde{\mathbf{V}}$ and $\tilde{\mathbf{I}}$ in the network model could significantly reduce nonlinearities of the model and the corresponding Jacobian matrix [1]. In this section, we propose a unified AC network branch model, a classic HVDC link model including its different control modes, and the interface model combining the above two models.

3.1. Unified AC network branch model

The AC network model of the PSE is more straight-forward than that of the conventional SE [1]. Replacing active and reactive power measurements with voltage and current phasor measurements reduces at least one order in each network model equation. The proposed model can be easily derived by using Kirchhoff's laws.

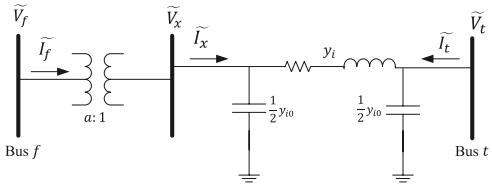

Fig. 1. AC line with transformer [17].

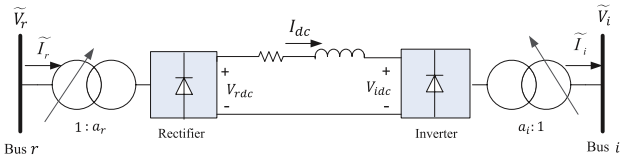

Fig. 2. A simplified DC link model [17].

As shown in Fig. 1, the model is built using not only lines with series impedance and shunt admittances, but also transformers. These components are sufficient to formulate most AC network models, which describe the relation between complex voltages on buses and complex currents flowing through the lines connected to these buses. This approach is similar to [1,2,17], but taking shunt admittances and transformers into account at the same time.

As shown in Fig. 1, the subscript $\boldsymbol{f}$ denotes the bus where current flows from and $\boldsymbol{t}$ is the bus where current flows to. The $\boldsymbol{i}$th line is represented by a series admittance y_i and shunt admittance y_{i0} in per unit. A transformer is represented by the off-nominal tap ratio $a : 1$. In the case of phase shifting transformers, a is a complex number. Consider a fictitious bus x between the ideal transformer and the line series admittance, thus, for the assumed current directions, we have

$$\tilde{V}_x = \frac{1}{a}\tilde{V}_f, \qquad \tilde{I}_x = a^*\tilde{I}_f.$$

The currents $\tilde{I}_x$ and $\tilde{I}_t$ are given by

$$\tilde{I}_x = -y_i\tilde{V}_t + \left(y_i + \frac{1}{2}y_{i0}\right)\tilde{V}_x, \qquad \tilde{I}_t = \left(y_i + \frac{1}{2}y_{i0}\right)\tilde{V}_t - y_i\tilde{V}_x.$$

Substituting for $\tilde{I}_x$ and $\tilde{V}_x$, we have

$$a^*\tilde{I}_f = -y_i\tilde{V}_t + \frac{1}{a}\left(y_i + \frac{1}{2}y_{i0}\right)\tilde{V}_f,$$

$$\tilde{I}_t = \left(y_i + \frac{1}{2}y_{i0}\right)\tilde{V}_t - \frac{1}{a}y_i\tilde{V}_f.$$

For $i \geq 2$, all the line parameters and measurements become vectors, then the above equations can be written in matrix form as:

$$\begin{bmatrix}\tilde{\mathbf{I}}_\mathbf{f}\\ \tilde{\mathbf{I}}_\mathbf{t}\end{bmatrix} = \begin{bmatrix}\mathbf{y_i} + \frac{1}{2}\mathbf{y_{i0}} & -\frac{\mathbf{y_i}}{\mathbf{a}^*}\\ -\frac{\mathbf{y_i}}{\mathbf{a}} & \mathbf{y_i} + \frac{1}{2}\mathbf{y_{i0}}\end{bmatrix}\begin{bmatrix}\tilde{\mathbf{V}}_\mathbf{f}\\ \tilde{\mathbf{V}}_\mathbf{t}\end{bmatrix}. \tag{5}$$

3.2. Classic HVDC link model including control modes

This subsection presents a classic HVDC link model for the PSE. It integrates DC voltages and currents with AC voltages and currents, which can be measured by PMUs, avoiding using active and reactive power transfer relations. In addition, corresponding control modes are introduced to supplement the network model.

A simplified DC link model is shown in Fig. 2, where a classic HVDC link couples two AC networks through a rectifier and an

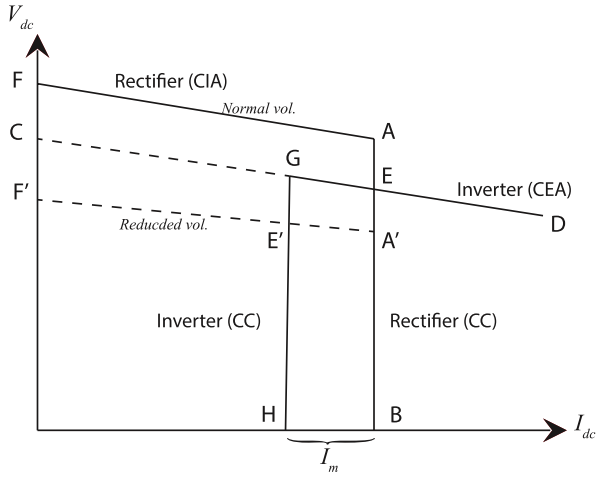

Fig. 3. Converter control steady-state characteristics [17,18].

inverter. The subscript **r** refers to the rectifier side of the DC link and **i** refers to the inverter side. For this classic HVDC link, the network equations are given by [15–18]:

$$\begin{cases} 0 = |\widetilde{I_r}| - K * \dfrac{3\sqrt{2}}{\pi} * a_r I_{dc} \\ 0 = V_{rdc} - K * \dfrac{3\sqrt{2}}{\pi} * a_r |\widetilde{V_r}| \cos(\theta_r - \delta_r) \\ 0 = V_{rdc} - K * \dfrac{3\sqrt{2}}{\pi} * a_r |\widetilde{V_r}| \cos\alpha + \dfrac{3}{\pi} X_r I_{dc} \\ 0 = |\widetilde{I_i}| - K * \dfrac{3\sqrt{2}}{\pi} * a_i I_{dc} \\ 0 = V_{idc} - K * \dfrac{3\sqrt{2}}{\pi} * a_i |\widetilde{V_i}| \cos(\theta_i - \delta_i) \\ 0 = V_{idc} - K * \dfrac{3\sqrt{2}}{\pi} * a_i |\widetilde{V_i}| \cos\delta + \dfrac{3}{\pi} X_i I_{dc} \\ 0 = I_{dc} - \dfrac{1}{R_{dc}} (V_{rdc} - V_{idc}), \end{cases} \tag{6}$$

where $K = 0.995$ is a coefficient for a twelve-pulse AC/DC converter; a_r and a_i are the tap ratios of the rectifier and inverter sides; α and δ[1] ($= \pi - \gamma$[2]) are the firing angle (also called ignition delay angle) and extinction delay angle, respectively; X_r and X_i are the transformer reactances of rectifier and inverter sides, respectively. $|\widetilde{V_r}|$ and θ_r are the magnitude and angle of $\widetilde{V_r}$; $|\widetilde{I_r}|$ and δ_r are the magnitude and angle of $\widetilde{I_r}$, which is the current phasor flowing from the AC side of rectifier to the DC link; the same quantities with subscript **i** apply to the inverter of the DC link. For the above seven equations, there are seven DC quantities of concern, which are V_{rdc}, V_{idc}, I_{dc}, $\cos\alpha$, $\cos\delta$, a_r, and a_i. Both AC and DC variables in (6) will become vectors when multiple classic HVDC links are installed in the system.

Eq. (6) characterizes classic HVDC links under steady state, without including the control models. In fact, including the HVDC control modes can contribute more information to the network model.

Generally, a classic HVDC link can control two variables at the rectifier and inverter, respectively: the transformer tap ratio a_r and the firing angle α on the rectifier side; the transformer tap ratio a_i and the extinction angle γ on the inverter side. The firing angle α keeps a normal operation range within 15° to 20° with a minimum limit about 5°. The extinction angle γ maintains a minimum limit of 15° for 50 Hz and 18° for 60 Hz. Controlling the firing/extinction angles is called grid/gate control, and is far more rapid (1–10 ms) than tap ratio control (5–6 s per step) [17]. Therefore, firing/extinction angle control is used initially for rapid actions, followed by tap ratios changing to restore the converter quantities, firing and extinction angles, to their normal ranges. Since the slow changes of tap ratios could be easily estimated [5], they are not included into the control mode equations. In this paper, we assume that the a_r and a_i are kept constant and the firing/extinction angles are used for control purposes.

The two most common control modes are briefly discussed below in order to develop the control mode equations, more details can be found in [17,18].

Rectifier current control mode (RCCM)

- When $\alpha > \alpha^{min}$, the rectifier maintains constant DC current by changing α. It is the normal constant current (CC) control mode (represented by *AB* in Fig. 3).
- When $\alpha = \alpha^{min}$, the rectifier maintains the constant ignition angle (CIA) control mode (represented by *FA*).
- The inverter always maintains a constant extinction angle (CEA) $\gamma = \gamma^{ref}$ control mode (represented by *CD*).

In this control mode, the intersection point *E* represents the normal operating condition.

Inverter current control mode (ICCM)

When the rectifier operates at a reduced voltage represented by $F'A'B$, *CD* representing the inverter's CEA operation would not intersect it. Therefore,

- The inverter maintains a constant current (represented by *GH*).
- The rectifier maintains a constant firing angle $\alpha = \alpha^{min}$ (represented by $F'A'$).

The intersection point E' represents the operating condition at a reduced rectifier voltage.

I_m in Fig. 3 denotes the current margin, which represents the difference between the rectifier current reference and inverter current reference. It is usually set at 10%–15% of the rated current to ensure that the two constant current characteristics do not cross each other due to errors in measurements or other causes [18].

Since the dynamics of the firing/extinction angle control are faster than PMU data reporting rates (20–50 ms per snapshot), we assume the dynamic control process (1–10 ms) is completed within several snapshots of the SE process. Therefore, the control mode equations used here only consider the equilibrium of each control mode, which are given by:

$$\begin{cases} 0 = C_1 * (I_{dc} - I_{dc}^{ref\,(re)}) \\ 0 = C_2 * (\gamma - \gamma^{ref}) \\ 0 = C_3 * (I_{dc} - I_{dc}^{ref\,(in)}) \\ 0 = C_4 * (\alpha - \alpha^{min}), \end{cases} \tag{7}$$

where $I_{dc}^{ref\,(re)}$ and $I_{dc}^{ref\,(in)}$ are the DC current references for the RCCM and ICCM, respectively; $\mathbf{C} = [C_1\ C_2\ C_3\ C_4]$ is the control mode index. $C_i = 1$ indicates the corresponding equation is activated, otherwise $C_i = 0$ indicates the corresponding equation will be removed out of the control mode equation set during the SE calculation. Hence, $\mathbf{C} = [1\ 1\ 0\ 0]$ and $\mathbf{C} = [0\ 0\ 1\ 1]$ refer to the RCCM and ICCM, respectively. Replacing γ and α with state

[1] δ here is a DC grid variable, which is different from the AC line current phasor angles, though they use the same notation to follow the previous work.

[2] γ is the extinction (advance) angle.

variables, (7) can be written as:

$$\begin{cases} 0 = C_1 * (I_{dc} - I_{dc}^{ref\,(re)}) \\ 0 = C_2 * (\cos\delta - \cos\delta^{ref}) \\ 0 = C_3 * (I_{dc} - I_{dc}^{ref\,(in)}) \\ 0 = C_4 * (\cos\alpha - \cos\alpha^{min}). \end{cases} \tag{8}$$

3.3. Interface model between DC Links and AC grids

Since a_r and a_i are treated as constant parameters, (6) only involves five DC states, V_{rdc}, V_{idc}, I_{dc}, $\cos\alpha$, and $\cos\delta$, and the AC voltage phasors $\widetilde{V}_r$, $\widetilde{V}_i$ and current phasors I_r, $\widetilde{I}_i$. However, current phasors $\widetilde{I}_r$, $\widetilde{I}_i$ are not included in the AC network model like $\widetilde{V}_r$ and $\widetilde{V}_i$. Hence, Kirchhoff's current law is applied at the buses to which the rectifier and the inverter are connected in order to formulate the current phasors $\widetilde{I}_r$, $\widetilde{I}_i$ with AC states as

$$\widetilde{I}_r = -\sum_{j=1}^{m} \widetilde{I}_{rj}, \qquad \widetilde{I}_i = \sum_{j=1}^{n} \widetilde{I}_{ij}, \tag{9}$$

where j denotes an AC bus to which bus r or i is connected through the AC line rj or ij; m (or n) denotes the number of buses which are connected to bus r (or i). As a result, the DC link and the AC grid have been interfaced through the voltage phasors $\widetilde{V}_r$, $\widetilde{V}_i$ and current phasors $\widetilde{I}_r$, $\widetilde{I}_i$.

These DC link model and interface model in the state estimator can adapt to various topologies of hybrid AC/DC grids. It can represent an embedded DC link in an existing AC grid or as an interconnection between two asynchronous AC grids. Future work will focus on extending the DC link model for multi-terminal DC (MTDC) grids [16].

4. PSE for hybrid AC/DC grids

The static network model proposed in Section 3 needs to be implemented in the measurement model as introduced in Section 2 for algebraic computation. This section illustrates how to formulate the measurement model as (2) and its corresponding Jacobian matrix. The state variable vector $\mathbf{x}$ for a hybrid AC/DC grid is

$$\mathbf{x} = [|\tilde{\mathbf{V}}| \;\; |\tilde{\mathbf{I}}| \;\; \boldsymbol{\theta} \;\; \boldsymbol{\delta} \;\; |\tilde{\mathbf{I}}_\mathbf{r}| \;\; |\tilde{\mathbf{I}}_\mathbf{i}| \;\; \boldsymbol{\delta}_\mathbf{r} \;\; \boldsymbol{\delta}_\mathbf{i} \;\; \mathbf{V_{rdc}} \; \mathbf{V_{idc}} \; \mathbf{I_{dc}} \;\; \cos\boldsymbol{\alpha} \;\; \cos\boldsymbol{\delta}]^\mathbf{T}.$$

Here voltage and current phasors are applied in polar form, i.e. absolute value and argument. Using phasors in polar form takes two significant advantages: (i) PMU measurements are provided in polar form so they can be directly used without form changes; (ii) more importantly, it allows angle bias detection and correction, which will be addressed in Section 5.3.

For a hybrid AC/DC grid, the network function $\mathbf{h}(\mathbf{x})$ is formulated as:

$$\mathbf{h}(\mathbf{x}) = \begin{bmatrix} \mathbf{h_{ac}}(\mathbf{x}) \\ \mathbf{h_{ad}}(\mathbf{x}) \\ \mathbf{h_{dc}}(\mathbf{x}) \end{bmatrix}. \tag{10}$$

Since phasors are applied in polar form, each linear equation in the AC network model (5) will be rewritten into two equations associated with trigonometric functions of the phasor angles. It is these trigonometric functions that introduce nonlinearity into the model. Based on Fig. 1, $\mathbf{h_{ac}}(\mathbf{x})$ can be formulated as

$$\mathbf{h_{ac}}(\mathbf{x}) = \begin{bmatrix} |\widetilde{\mathbf{V}}_\mathbf{f}||\mathbf{y_{ff}}|\cos(\boldsymbol{\theta}_\mathbf{f} + \boldsymbol{\phi}_\mathbf{ff}) - |\widetilde{\mathbf{V}}_\mathbf{t}||\mathbf{y_{ft}}|\cos(\boldsymbol{\theta}_\mathbf{t} + \boldsymbol{\phi}_\mathbf{ft}) - |\widetilde{\mathbf{I}}_\mathbf{f}|\cos\boldsymbol{\delta}_\mathbf{f} \\ |\widetilde{\mathbf{V}}_\mathbf{f}||\mathbf{y_{ff}}|\sin(\boldsymbol{\theta}_\mathbf{f} + \boldsymbol{\phi}_\mathbf{ff}) - |\widetilde{\mathbf{V}}_\mathbf{t}||\mathbf{y_{ft}}|\sin(\boldsymbol{\theta}_\mathbf{t} + \boldsymbol{\phi}_\mathbf{ft}) - |\widetilde{\mathbf{I}}_\mathbf{f}|\sin\boldsymbol{\delta}_\mathbf{f} \\ |\widetilde{\mathbf{V}}_\mathbf{f}||\mathbf{y_{tf}}|\cos(\boldsymbol{\theta}_\mathbf{f} + \boldsymbol{\phi}_\mathbf{tf}) - |\widetilde{\mathbf{V}}_\mathbf{t}||\mathbf{y_{tt}}|\cos(\boldsymbol{\theta}_\mathbf{t} + \boldsymbol{\phi}_\mathbf{tt}) - |\widetilde{\mathbf{I}}_\mathbf{t}|\cos\boldsymbol{\delta}_\mathbf{t} \\ |\widetilde{\mathbf{V}}_\mathbf{f}||\mathbf{y_{tf}}|\sin(\boldsymbol{\theta}_\mathbf{f} + \boldsymbol{\phi}_\mathbf{tf}) - |\widetilde{\mathbf{V}}_\mathbf{t}||\mathbf{y_{tt}}|\sin(\boldsymbol{\theta}_\mathbf{t} + \boldsymbol{\phi}_\mathbf{tt}) - |\widetilde{\mathbf{I}}_\mathbf{t}|\sin\boldsymbol{\delta}_\mathbf{t} \end{bmatrix}.$$

In addition,

$$\mathbf{h_{ad}}(\mathbf{x}) = \begin{bmatrix} |\widetilde{\mathbf{I}}_\mathbf{r}|\cos\boldsymbol{\delta}_\mathbf{r} + \sum_{\mathbf{j=1}}^{\mathbf{m}} |\widetilde{\mathbf{I}}_\mathbf{rj}|\cos\boldsymbol{\delta}_\mathbf{rj} \\ |\widetilde{\mathbf{I}}_\mathbf{r}|\sin\boldsymbol{\delta}_\mathbf{r} + \sum_{\mathbf{j=1}}^{\mathbf{m}} |\widetilde{\mathbf{I}}_\mathbf{rj}|\sin\boldsymbol{\delta}_\mathbf{rj} \\ |\widetilde{\mathbf{I}}_\mathbf{i}|\cos\boldsymbol{\delta}_\mathbf{i} - \sum_{\mathbf{j=1}}^{\mathbf{n}} |\widetilde{\mathbf{I}}_\mathbf{ij}|\cos\boldsymbol{\delta}_\mathbf{ij} \\ |\widetilde{\mathbf{I}}_\mathbf{i}|\sin\boldsymbol{\delta}_\mathbf{i} - \sum_{\mathbf{j=1}}^{\mathbf{n}} |\widetilde{\mathbf{I}}_\mathbf{ij}|\sin\boldsymbol{\delta}_\mathbf{ij} \end{bmatrix},$$

$$\mathbf{h_{dc}}(\mathbf{x}) = \begin{bmatrix} K * \frac{3\sqrt{2}}{\pi} * \mathbf{a_r}\mathbf{I_{dc}} - |\widetilde{\mathbf{I}}_\mathbf{r}| \\ K * \frac{3\sqrt{2}}{\pi} * \mathbf{a_r}|\widetilde{\mathbf{V}}_\mathbf{r}|\cos(\boldsymbol{\theta}_\mathbf{r} - \boldsymbol{\delta}_\mathbf{r}) - \mathbf{V_{rdc}} \\ K * \frac{3\sqrt{2}}{\pi} * \mathbf{a_r}|\widetilde{\mathbf{V}}_\mathbf{r}|\cos\boldsymbol{\alpha} - \frac{3}{\pi}\mathbf{X_r}\mathbf{I_{dc}} - \mathbf{V_{rdc}} \\ K * \frac{3\sqrt{2}}{\pi} * \mathbf{a_i}I_{dc} - |\widetilde{\mathbf{I}}_\mathbf{i}| \\ K * \frac{3\sqrt{2}}{\pi} * \mathbf{a_i}|\widetilde{\mathbf{V}}_\mathbf{i}|\cos(\boldsymbol{\theta}_\mathbf{i} - \boldsymbol{\delta}_\mathbf{i}) - \mathbf{V_{idc}} \\ K * \frac{3\sqrt{2}}{\pi} * \mathbf{a_i}|\widetilde{\mathbf{V}}_\mathbf{i}|\cos\boldsymbol{\delta} - \frac{3}{\pi}\mathbf{X}_i\mathbf{I_{dc}} - \mathbf{V_{idc}} \\ \mathbf{V_{rdc}} - \mathbf{V_{idc}} - R_\mathbf{dc}\mathbf{I_{dc}} \\ \mathbf{C_1} * (\mathbf{I_{dc}} - \mathbf{I_{dc}^{ref(re)}}) + \mathbf{C_3} * (\mathbf{I_{dc}} - \mathbf{I_{dc}^{ref(in)}}) \\ \mathbf{C_2} * (\mathbf{cos}\delta - \mathbf{cos}\delta^{\mathbf{ref}}) + \mathbf{C_4} * (\mathbf{cos}\alpha - \mathbf{cos}\alpha^{\mathbf{min}}) \end{bmatrix}.$$

The second part of the measurement model can be expressed as:

$$\mathbf{x} - \mathbf{z} = \begin{bmatrix} \mathbf{x_{ac}} - \mathbf{z_{ac}} \\ \mathbf{x_{ad}} - \mathbf{z_{ad}} \\ \mathbf{x_{dc}} - \mathbf{z_{dc}} \end{bmatrix}, \tag{11}$$

where

$$\mathbf{x_{ac}} - \mathbf{z_{ac}} = \left[|\widetilde{\mathbf{V}}| - |\widetilde{\mathbf{V}^\mathbf{m}}| \quad |\widetilde{\mathbf{I}}| - |\widetilde{\mathbf{I}^\mathbf{m}}| \quad \boldsymbol{\theta} - \boldsymbol{\theta}^\mathbf{m} \quad \boldsymbol{\delta} - \boldsymbol{\delta}^\mathbf{m}\right]^\mathbf{T},$$

$$\mathbf{x_{ad}} - \mathbf{z_{ad}} = \left[|\widetilde{\mathbf{I}}_\mathbf{r}| - |\widetilde{\mathbf{I}}_\mathbf{r}^\mathbf{m}| \quad |\widetilde{\mathbf{I}}_\mathbf{i}| - |\widetilde{\mathbf{I}}_\mathbf{i}^\mathbf{m}| \quad \boldsymbol{\delta}_\mathbf{r} - \boldsymbol{\delta}_\mathbf{r}^\mathbf{m} \quad \boldsymbol{\delta}_\mathbf{i} - \boldsymbol{\delta}_\mathbf{i}^\mathbf{m}\right]^\mathbf{T},$$

$$\mathbf{x_{dc}} - \mathbf{z_{dc}} = \begin{bmatrix} \mathbf{V_{rdc}} - \mathbf{V_{rdc}^m} \\ \mathbf{V_{idc}} - \mathbf{V_{idc}^m} \\ \mathbf{I_{dc}} - \mathbf{I_{dc}^m} \\ \cos\alpha - \cos\alpha^\mathbf{m} \\ \cos\delta - \cos\delta^\mathbf{m} \end{bmatrix}.$$

The PSE Jacobian matrix for hybrid AC/DC grid is shown as: (see the equation in Box I).

where

$$\frac{\partial \mathbf{h_{ad}}(\mathbf{x})}{\partial |\widetilde{\mathbf{I}}|} = \begin{bmatrix} \cos\delta_{rj} & \text{or} & 0 \\ \sin\delta_{rj} & \text{or} & 0 \\ \cos\delta_{ij} & \text{or} & 0 \\ \sin\delta_{ij} & \text{or} & 0 \end{bmatrix},$$

$$\frac{\partial \mathbf{h_{ad}}(\mathbf{x})}{\partial \boldsymbol{\delta}} = \begin{bmatrix} -|\widetilde{I}_{rj}|\sin\delta_{rj} & \text{or} & 0 \\ |\widetilde{I}_{rj}|\cos\delta_{rj} & \text{or} & 0 \\ |\widetilde{I}_{ij}|\sin\delta_{ij} & \text{or} & 0 \\ -|\widetilde{I}_{ij}|\cos\delta_{ij} & \text{or} & 0 \end{bmatrix},$$

$$\frac{\partial \mathbf{h_{dc}}(\mathbf{x})}{\partial |\widetilde{\mathbf{V}}|} = \begin{bmatrix} 0 & & \\ K_1 * a_r\cos(\theta_r - \delta_r) & \text{or} & 0 \\ K_1 * a_r\cos\alpha & \text{or} & 0 \\ 0 & & \\ K_1 * a_i\cos(\theta_i - \delta_i) & \text{or} & 0 \\ K_1 * a_i\cos\delta & \text{or} & 0 \\ 0 & & \\ 0 & & \\ 0 & & \end{bmatrix},$$

$$\mathbf{H}(\widetilde{\mathbf{x}}) = \left[\begin{array}{cccc|cc|c} \frac{\partial \mathbf{h_{ac}(x)}}{\partial |\widetilde{\mathbf{V}}|} & \frac{\partial \mathbf{h_{ac}(x)}}{\partial |\widetilde{\mathbf{I}}|} & \frac{\partial \mathbf{h_{ac}(x)}}{\partial \theta} & \frac{\partial \mathbf{h_{ac}(x)}}{\partial \delta} & \multicolumn{2}{c|}{\mathbf{0}} & \mathbf{0} \\ \hline \mathbf{0} & \frac{\partial \mathbf{h_{ad}(x)}}{\partial |\widetilde{\mathbf{I}}|} & \mathbf{0} & \frac{\partial \mathbf{h_{ad}(x)}}{\partial \delta} & \begin{array}{c}\cos\delta_{\mathbf{r}} \\ \sin\delta_{\mathbf{r}}\end{array} & \begin{array}{c}-|\widetilde{\mathbf{I}}_{\mathbf{r}}|\sin\delta_{\mathbf{r}} \\ |\widetilde{\mathbf{I}}_{\mathbf{r}}|\cos\delta_{\mathbf{r}}\end{array} & \mathbf{0} \\ & & & & \begin{array}{c}\cos\delta_{\mathbf{i}} \\ \sin\delta_{\mathbf{i}}\end{array} & \begin{array}{c}-|\widetilde{\mathbf{I}}_{\mathbf{i}}|\sin\delta_{\mathbf{i}} \\ |\widetilde{\mathbf{I}}_{\mathbf{i}}|\cos\delta_{\mathbf{i}}\end{array} & \\ \hline \frac{\partial \mathbf{h_{dc}(x)}}{\partial |\widetilde{\mathbf{V}}|} & \mathbf{0} & \frac{\partial \mathbf{h_{dc}(x)}}{\partial \theta} & \mathbf{0} & -\mathbf{I} & K_1 * \mathbf{a_r}|\widetilde{\mathbf{V}}_{\mathbf{r}}|\sin(\theta_{\mathbf{r}} - \delta_{\mathbf{r}}) & \frac{\partial \mathbf{h_{dc}(x)}}{\partial \mathbf{x_{dc}}} \\ & & & & -\mathbf{I} & K_1 * \mathbf{a}_i|\widetilde{\mathbf{V}}_{\mathbf{i}}|\sin(\theta_{\mathbf{i}} - \delta_{\mathbf{i}}) & \\ \hline \multicolumn{3}{c}{\begin{array}{c}\mathbf{I} \\ \mathbf{0} \\ \mathbf{0}\end{array}} & & \multicolumn{2}{c}{\begin{array}{c}\mathbf{0} \\ \mathbf{I} \\ \mathbf{0}\end{array}} & \begin{array}{c}\mathbf{0} \\ \mathbf{0} \\ \mathbf{I}\end{array} \end{array}\right], \quad (12)$$

Box I.

$$\frac{\partial \mathbf{h_{dc}(x)}}{\partial \boldsymbol{\theta}} = \begin{bmatrix} -K_1 * a_r \sin(\theta_r - \delta_r) & \text{or} & 0 \\ -K_1 * a_i \sin(\theta_i - \delta_i) & \text{or} & 0 \end{bmatrix},$$

$$\frac{\partial \mathbf{h_{dc}(x)}}{\partial \mathbf{x_{dc}}} = \begin{bmatrix} 0 & 0 & K_1 a_r & 0 & 0 \\ -1 & 0 & 0 & 0 & 0 \\ -1 & 0 & -K_2 X_r & K_1 * a_r|\widetilde{V}_r| & 0 \\ 0 & 0 & K_1 a_i & 0 & 0 \\ 0 & -1 & 0 & 0 & 0 \\ 0 & -1 & -K_2 X_i & 0 & K_1 * a_i|\widetilde{V}_i| \\ 1 & -1 & -R_{dc} & 0 & 0 \\ 0 & 0 & C_1 + C_3 & 0 & 0 \\ 0 & 0 & 0 & C_4 & C_2 \end{bmatrix},$$

$$K_1 = 0.995 * \frac{3\sqrt{2}}{\pi}, \qquad K_2 = \frac{3}{\pi}.$$

As shown by (12), the nonlinearities in the Jacobian matrix are much fewer than those in the Jacobian matrix of a conventional SE, which will significantly reduce the computation load. The high degree of sparsity also helps to decrease the computational effort substantially. Hence, the PSE could follow the trajectory of the power system and should sanitize data quickly to support other applications.

5. Considerations for practical application

In the perfect condition for the PSE, PMUs would be installed at all buses so all the bus voltage and line current phasors are measured. The system would be fully observable and would have high redundancy; measurement noises would be too small to affect the estimation, so they would be neglected; additionally, PMU measurements would be perfectly synchronized by GPS clocks in a large-scale deployments.

However, in real life this condition cannot be met, and all of the above issues have to be carefully considered since they may affect the SE's performance. Therefore, prior to implementing the proposed PSE algorithm, all these issues of it need to be carefully assessed. This section discusses how to analyze system observability with PMUs and the effect of redundancy, what is the allowable measurement noise level of PMUs and DC grid measurements, and how to deal with the phase mismatch owing to imperfect PMUs synchronization.

5.1. Observability analysis and measurement redundancy

Generally, observability analysis aims to determine whether there are observable islands within the network, and isolate observable islands. System observability can be analyzed in two main approaches: topological and/or numerical methods. Basic topological algorithms for conventional SEs can be found in [1,2,19]. A non-iterative numerical algorithm is proposed in [20]. In addition, observability often acts as the criterion for PMU placement in a power system, which aims to maximize system observability with a minimum number of PMUs. If full observability for an entire network is required, the algorithms in [21–25] may be used for adding new PMUs.

However, observability analysis in this paper is performed for each individual island, aiming to define whether this island is observable or not as a portion of the power network, and then developing independent state estimator models for each island to be solved. Strictly defining observable islands for an entire system is out of this paper's scope.

Since PMU phasor measurements for PSE replace power flow and power injection measurements from SCADA, new topological rules for AC systems are as follow [26,27]:

- R1: A bus with a PMU installed and any line extending from the bus are observed.
- R2: Any bus that is incident to an observed line connected to an observed bus is observed.
- R3: Any line joining two observed buses is observed.
- R4: If all the lines incident to an observed bus are observed, save one, then all of the lines incident to that bus are observed.
- R5: Any bus incident only to observed lines is observed.

Note that R4 holds based on the usage of the PSE bus modeling method as shown in Fig. 4(a), which requires that the power system model must account for the bus at the load side (Bus B) and any other transmission equipment (e.g. a transformer located on line 4) before they are connected to the substation bus (Bus A). This bus model avoid the potential unobservable problems for non-zero

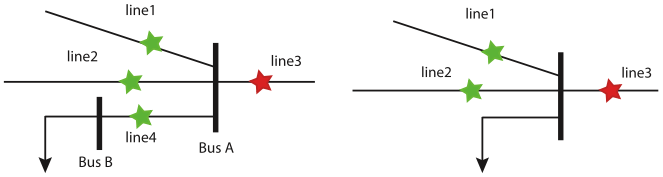

(a) PSE. (b) Conventional SE.

Fig. 4. Non-zero injection bus modeling methods.

injection buses, which exit when applying R4 on the conventional SE bus model as shown in Fig. 4(b). As illustrated by Fig. 4(a), green stars represent the observable lines and according to R4 the last line with red star will be observable. While in Fig. 4(b), R4 does not hold due to the unknown injection.

Therefore, with PSE bus modeling method R4 allows us to consider this type of network topology, i.e. the connection between a load or a generator to the high voltage system through a transformer. This approach suits for non-zero injection buses, additionally, it is easy to implement and makes the model more organized.

An annotated example for the above definition of observability can be found in [27].

To define observability rules for classic HVDC links, it is necessary to account for all the states involved in each link. There are five DC states to be estimated, together with four AC states ($|\widetilde{V}_r|$, $|\widetilde{V}_i|$, θ_r, θ_i), and four AC/DC interface states ($|\widetilde{I}_r|$, $|\widetilde{I}_i|$, δ_r, δ_i). Observe that for every set of DC link equations, (6) and (8), there are 13 states involved. Therefore, the hybrid AC/DC observability algorithm is extended by considering the DC network model:

- R6: The DC link is observable if all DC states are measured by metering devices.
- R7: If the DC states are not fully measured, at least 4 of 13 states involved in each link model have to be known in order to make all the DC states observable. Note that the AC/DC interface state variables among the four measurements do not have to be measured directly. They can also be accounted as known states by being calculated from AC measurements.

However, not all combinations of four measurements will suffice. First, these four measurements should not contain I_{dc} and $\cos\delta$ for RCCM, or I_{dc} and $\cos\alpha$ for ICCM since the control mode equations have already provided references for the above state variables. Second, the four measurements should not all come from only the rectifier side or only the inverter side. In addition, any of the four measured state variables should not be possible to be calculated by the other three measurements. Providing a classic HVDC link under RCCM, (6) and (8) can be reduced to a five-equation set as follows:

$$\begin{cases} 0 = \mathbf{f_1}(|\widetilde{\mathbf{V}}_\mathbf{r}|, \boldsymbol{\theta}_\mathbf{r}, \boldsymbol{\delta}_\mathbf{r}, \mathbf{V_{rdc}}) \\ 0 = \mathbf{f_2}(|\widetilde{\mathbf{V}}_\mathbf{r}|, \cos\alpha, \mathbf{V_{rdc}}) \\ 0 = \mathbf{f_3}(|\widetilde{\mathbf{V}}_\mathbf{i}|, \boldsymbol{\theta}_\mathbf{i}, \boldsymbol{\delta}_\mathbf{i}, \mathbf{V_{idc}}) \\ 0 = \mathbf{f_4}(|\widetilde{\mathbf{V}}_\mathbf{i}|, \mathbf{V_{idc}}) \\ 0 = \mathbf{f_5}(\mathbf{V_{rdc}}, \mathbf{V_{idc}}). \end{cases} \tag{13}$$

Based on (13), the combinations can be divided in two types: two measurements from the rectifier side and two from the inverter side, three measurements from the rectifier side and one from the inverter side. For the first type, all the combinations can be inferred by the following steps:

- S1: The first measurement selected from inverter side can be $|\widetilde{\mathbf{V}}_\mathbf{i}|$ or $\mathbf{V_{idc}}$. Knowing either of them can calculate the other one by using $\mathbf{f_4}$. Moreover, $\mathbf{V_{rdc}}$ will be known sequentially by $\mathbf{f_5}$.
- S2: Knowing either $\boldsymbol{\theta}_\mathbf{i}$ or $\boldsymbol{\delta}_\mathbf{i}$ can calculate the other. So far, all the states from the inverter side have been known.

Table 1
Proper combinations of four measurements to make a classic HVDC link observable.

$\lvert\widetilde{V}_r\rvert$	θ_r	δ_r	V_{rdc}	$cos\alpha$	$\lvert\widetilde{V}_i\rvert$	θ_i	δ_i	V_{idc}
*	*				*	*		
	*	*			*	*		
	*			*	*	*		
*		*			*	*		
		*		*	*	*		
*	*				*		*	
	*	*			*		*	
	*			*	*		*	
*		*			*		*	
		*		*	*		*	
*	*					*		*
	*	*				*		*
	*			*		*		*
*		*				*		*
		*		*		*		*
*	*						*	*
	*	*					*	*
	*			*			*	*
*		*					*	*
		*		*			*	*
*	*			*		*		
*	*			*			*	
*	*	*				*		
*	*	*					*	
*	*		*			*		
*	*		*				*	
*		*	*			*		
*		*	*				*	
*		*		*		*		
*		*		*			*	
	*		*	*		*		
	*		*	*			*	
		*	*	*		*		
		*	*	*			*	
	*	*	*			*		
	*	*	*				*	
	*	*		*		*		
	*	*		*			*	

- S3: Since $\mathbf{V_{rdc}}$ has been calculated, there are two equation $\mathbf{f_1}$ and $\mathbf{f_2}$ for four unknown states, which are $|\widetilde{\mathbf{V}}_\mathbf{r}|$, $\boldsymbol{\theta}_\mathbf{r}$, $\boldsymbol{\delta}_\mathbf{r}$, and $\cos\boldsymbol{\alpha}$. Therefore, any two of the four states can be selected, except for choosing $|\widetilde{\mathbf{V}}_\mathbf{r}|$ and $\cos\boldsymbol{\alpha}$ simultaneously.
- S4: In total, the number of combinations is $2\times2\times(C_4^2-1) = 20$.

For the second type, the steps are as follows:

- S1: Select any three measurements among five states in the rectifier side except for selecting $|\widetilde{\mathbf{V}}_\mathbf{r}|$, $\cos\alpha$, $\mathbf{V_{rdc}}$ together. Hence, all the states in the rectifier side can be calculated associated with $\mathbf{f_1}$ and $\mathbf{f_2}$.
- S2: $\mathbf{V_{idc}}$ will be sequentially known by $\mathbf{f_5}$ and then $|\widetilde{\mathbf{V}}_\mathbf{i}|$ is known by $\mathbf{f_4}$.
- S3: Either $\boldsymbol{\theta}_\mathbf{i}$ or $\boldsymbol{\delta}_\mathbf{i}$ can calculate the other. So far, all the states from the inverter side have been known.
- S4: In total, the number of combinations is $(C_5^3 - 1) \times 2 = 18$.

All the proper combinations of four measurements to make a classic HVDC link observable are shown in Table 1. The upper part of Table 1 presents the first type of combinations, whereas,

Table 2
σ_{max} for different PMU variables.

$\|V\|$	0.02% of reading or 0.002% range
$\|I\|$	0.03% of reading or 0.003% range
θ and δ	0.01° or 10% of range minimum

the lower part is for the second type of combinations. Since PMUs measure synthetic magnitudes and angles together in phasor form, thus, in reality extra measurements out of each combination might be obtained incidentally. For instance, when using the combination of $\boldsymbol{\theta_r}$, $\boldsymbol{\delta_r}$, $|\widetilde{\mathbf{V}}_\mathbf{i}|$, and $\boldsymbol{\theta_i}$; $|\widetilde{\mathbf{V}}_\mathbf{r}|$, and $|\widetilde{\mathbf{I}}_\mathbf{r}|$ would be known automatically when $\boldsymbol{\theta_r}$, $\boldsymbol{\delta_r}$ are measured or calculated.

As indicated by the red marks in Table 1, in the case of no measurement redundancy, the DC states can still be computed even without any DC measurement. This brings a great advantage since AC measurements can be easily obtained by PMUs. When measurements are redundant, this can be taken as an advantage for cross-validation [28], as discussed in Section 5.3. In addition, rectifier and inverter tap ratios can also be included as DC states when necessary since there are four more equations than the number of DC states.

A complementary approach is to examine the Jacobian matrix of the hybrid AC/DC grid, which is referred as to the numerical method.

$$rank((\mathbf{H})^\mathbf{T}(\mathbf{H})) = N_x, \tag{14}$$

where $\mathbf{H}(\mathbf{x})$ is the Jacobian matrix; and N_x represents the number of state variables. Generally, the more rows that the Jacobian matrix has with respect to the number of columns, the higher the redundancy offered by the PSE. As mentioned in [1,2,5], measurement redundancy is crucial for bad data detection and identification.

When a measurement is lost, the corresponding measurement row in the measurement model equation, the Jacobian matrix $\mathbf{H}(\mathbf{x})$, and its weighting in weighting matrix $\mathbf{W}(\mathbf{x})$ will be removed. As long as (14) holds, all the states can be estimated by using the nonlinear WLS algorithm.

A simulation study for the low measurement redundancy scenario is presented in Section 6.3 to illustrate its effect on PSE accuracy.

5.2. Measurement noise and the choice of weightings

In reality, it is impossible to avoid measurement noises due to PMU metering and other causes. The standard uncertainty (σ) for each measurement is proportional to the specified maximum uncertainty (σ_{max}) of the PMU with a coefficient of $\frac{1}{\sqrt{3}}$ [29,30]. In the IEEE standard C37.242-2013 [31], PMUs have the capability of providing the following accuracy:

1. Time tagging with accuracy better than 1 μs (or equivalently 0.02° of phase at 60 Hz).
2. Magnitude accuracy of 0.1% or better.

However, in reality the σ_{max} varies according to each PMUs manufacturer. For instance, [32] provides the accuracies shown in Table 2.

In addition, it is assumed that the DC measurements have a σ_{max} of 0.01% of reading or 0.001% range. Then the σ_{max} values in Table 2 are used and transferred into signal-to-noise ratios (SNRs) by using (15) in order to add Gaussian noise to the true values.

$$SNR = 10 * log_{10}\left(\frac{\sqrt{3}}{\sigma_{max}}\right)^2 \text{dB}. \tag{15}$$

As discussed in Section 2, the weighting in the WLS algorithm would be optimal if the inverse of the corresponding measurement covariance is used. Therefore, the SNRs and the weightings for different measurements can be calculated as shown in Table 3.

Table 3
SNRs and weightings for different measurements.

Meas.	SNR (dB)	Weighting
$\|V\|$	78.75	$7.5 * 10^7$
$\|I\|$	75.23	$3.3 * 10^7$
θ and δ	79.93	$9.8 * 10^7$
DC states	84.77	$3 * 10^8$

The weightings for network model equations depend on the modeling accuracy for each component. A simulation test of applying AC and DC measurement noises and corresponding weightings into the PSE is show in Section 6.3, where the weightings for network model equations are all equal to the highest measurement weighting.

5.3. Angle bias detection and correction by PSE

Angle biases (or shifts) emerge due to imperfect synchronization or incorrect time-tagging by the PMUs [4,6,33]. These phase angle errors have been observed from recorded data in several utilities [4,5]. Paper [34] presents two time skew cases that result in angle biases. In one case, the GPS signal cable was loosely connected so the signal was intermittent. Thus, the PMU time was not accurate, resulting in spikes on top of the correct angle values. The other case of angle bias occurred due to drifting of the internal clock.

Different from measurement errors, angle bias does not have a normal distribution and its deviation varies within 1∼2 degrees, even 20° in some extreme cases. In addition, angle bias could last for a few snapshots, which may contaminate other measurements.

Since in the PSE, magnitudes and angles are separated as independent states, angle biases can be detected by using redundant measurements [4]. The vector of angle bias variables $\boldsymbol{\Omega}$ is included in the state vector as

$$\mathbf{x} = [|\widetilde{\mathbf{V}}|\ \ |\widetilde{\mathbf{I}}|\ \ \boldsymbol{\theta}\ \ \boldsymbol{\delta}\ \ |\widetilde{\mathbf{I}}_\mathbf{r}|\ \ |\widetilde{\mathbf{I}}_\mathbf{i}|\ \ \boldsymbol{\delta_r}\ \ \boldsymbol{\delta_i}\ \mathbf{V_{rdc}}\ \mathbf{V_{idc}}\ \mathbf{I_{dc}}\ \cos\boldsymbol{\alpha}\ \cos\boldsymbol{\delta}\ \boldsymbol{\Omega}]^\mathbf{T}$$

where

$$\boldsymbol{\Omega} = [\boldsymbol{\Omega_\theta}\ \ \boldsymbol{\Omega_\delta}\ \ \boldsymbol{\Omega_r}\ \ \boldsymbol{\Omega_i}].$$

The voltage and current angles in the AC grid measurement model become

$$\boldsymbol{\theta} - \boldsymbol{\theta}^\mathbf{m} + \boldsymbol{\Omega_\theta} \quad \text{and} \quad \boldsymbol{\delta} - \boldsymbol{\delta}^\mathbf{m} + \boldsymbol{\Omega_\delta}.$$

Similarly, the current angles in the interface measurement model become

$$\boldsymbol{\delta_r} - \boldsymbol{\delta}_\mathbf{r}^\mathbf{m} + \boldsymbol{\Omega_r} \quad \text{and} \quad \boldsymbol{\delta_i} - \boldsymbol{\delta}_\mathbf{i}^\mathbf{m} + \boldsymbol{\Omega_i}.$$

In order to correct the angle bias, it is required that

$$rank((\mathbf{H})^\mathbf{T}(\mathbf{H})) = N_x + N_\Omega, \tag{16}$$

where N_Ω represents the number of angle bias auxiliary state variables.

This approach has been defined more formally in the control literature, and it has been termed as cross-validation. Mathematical proofs for cross-validation rules, as used in this paper, are available in [28].

The angle bias variable $\boldsymbol{\Omega}$ greatly facilitates angle bias correction. Compared to common bad date detection and correction methods, such as by using normalized residuals [1], it does not need to perform additional calculations or to define a threshold to determine bad data. In addition, it avoids the risk that the largest normalized residual method may fail in the detection of gross errors for the measurements that have a large undetectable

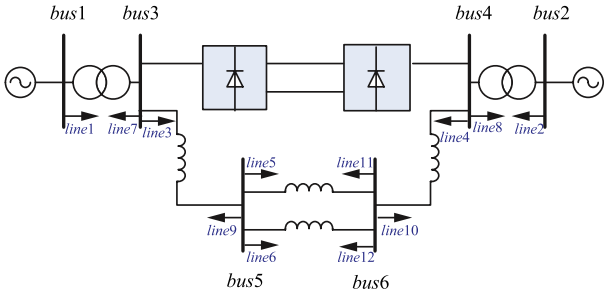

Fig. 5. Six-bus hybrid AC/DC system.

component [35]. In fact, this angle bias correction gives a huge flexibility for correcting angle bias no matter how large the bias is. The requirement, however, is to have enough redundancy to accommodate the angle bias variables $\boldsymbol{\Omega}$. Hence, if the power system has high measurement redundancy, this approach would be suitable.

Paper [6] applies the same algorithm for magnitude error detection and correction. However, the authors believe it is not necessary to use this method to correct magnitude errors, because the incorrect time tagging issues normally do not give rise to deviations in the magnitude measurements. It is not worth scarifying measurements redundancy to detect and correct minor magnitude errors.

A simulation test for the angle bias scenario is show in Section 6.5 to illustrate this method's performance.

6. Study cases

In this section, we apply the proposed PSE algorithm on the synthetic measurements from both a six-bus hybrid AC/DC system and the KTH-NORDIC32 hybrid AC/DC system [11]. Test scenarios for illustrating the practical issues are also performed. The synthetic measurements used for off-line PSE computations were obtained by running time-domain simulations using the Power System Analysis Toolbox (PSAT) [36]. The time-domain simulations were run with a time-step (Δt) of 20 ms (which corresponds to a 50 samples/second—PMUs reporting rate), and each solution at Δt was synthesized as a measurement snapshot; hence, performing time-domain simulations allows to expose the system dynamics for the model in the synthesized data.

In order to illustrate the performance of the proposed PSE, in Sections 6.1 and 6.2, all the weightings for both network equations and measurements are assumed to be 1, and full measurement observability is assumed. The following three subsections present simulation results for a scenario with low measurement redundancy, a scenario considering realistic measurement noises and corresponding weightings, and a scenario where angle bias correction is performed. At last, simulation time and computation performance is discussed.

6.1. Simulation results for a six-bus hybrid AC/DC system

The diagram for a six-bus hybrid AC/DC system is shown in Fig. 5.

The line breaker located on line 4 between bus 4 and 6 was opened at $t = 5$ s and after three cycles it was re-closed at $t = 5.06$ s. The DC link was under the normal operation condition with $I_{dc}^{ref} = 0.506$ p.u. and $\cos\delta^{ref} = 0.951$ p.u. for RCCM. Phasor measurements in polar form were acquired for a period of 20 s.

The PSE process starts with building up the static network model. First, the state vector for the six-bus hybrid AC/DC system is defined as follows

$$\mathbf{x} = [|\widetilde{V}_1|,\ |\widetilde{V}_2|\ \ldots\ |\widetilde{V}_6|,\ \theta_1,\ \theta_2,\ \ldots\ \theta_6,\ |\widetilde{I}_1|,\ |\widetilde{I}_2|\ \ldots\ |\widetilde{I}_{12}|,\ \delta_1,\ \delta_2,\ \ldots\ \delta_{12}, |\widetilde{I}_r|,\ |\widetilde{I}_i|,\ \delta_r,\ \delta_i,\ V_{rdc},\ V_{idc},\ I_{dc},\ \cos\alpha,\ \cos\delta]^T.$$

Then, based on network configuration and parameters, and the unified AC network branch model and the classic HVDC link model, the whole network model is built.

The acquired measurements for all the state variables and network model are applied to the measurement model as in (2). To minimize the errors of the PSE, the performance index (3) must be minimized by using the WLS algorithm. (4) gives the iteration procedure, where the Jacobian matrix can be calculated by using (12). Fig. 6 shows the SE computation results for one single snapshot, and Fig. 7 is for multiple snapshots.

Since the network model for the PSE is relatively similar to the model in PSAT, the residuals for one single snapshot are extremely small, lower than 10^{-14} p.u. However, when the system was subject to a perturbation, the PSE residuals increased as shown in Fig. 7. This is because the topology of the system changes when the perturbation occurs; however, the PSE model remains the same and is not adapted to the change accordingly. This indeed explains why in Fig. 7 the SE performance decreased at the instance when the breaker was opened and then came back to a normal level after the breaker was closed. Topology processing or network model updating is out of the scope of this paper. Nevertheless, the SE residuals are still within acceptable error range, including at the peaks occurring instant when the perturbation happened.

6.2. Simulation results for the KTH-NORDIC32 hybrid AC/DC system

The diagram for the KTH-NORDIC32 hybrid AC/DC system is shown in Fig. 8. This system is a conceptualization of the Swedish power system and its neighbors. Its precursors are the CIGRE "Nordic 32A" test network developed by K. Walve [37] and a system data set proposed by T. Van Cutsem [38]. In [39] some adjustments to the system model and its parameters were made, since then the model is referred to as the KTH-NORDIC32 system [39]. In order to test the hybrid AC/DC PSE, a 400 kV classic

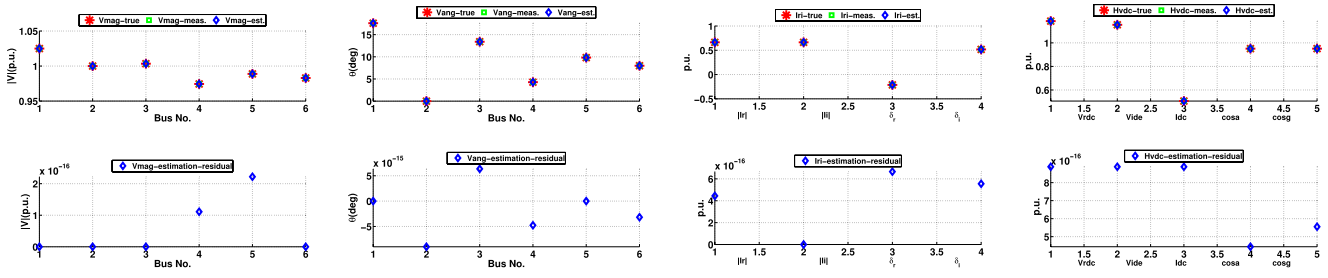

(a) Voltage magnitudes at all the buses for one snapshot.

(b) Voltage angles for one snapshot (bus 2 is the slack bus).

(c) AC/DC interface states for one snapshot.

(d) DC states for one snapshot.

Fig. 6. PSE for the six-bus hybrid AC/DC system for a single snapshot.

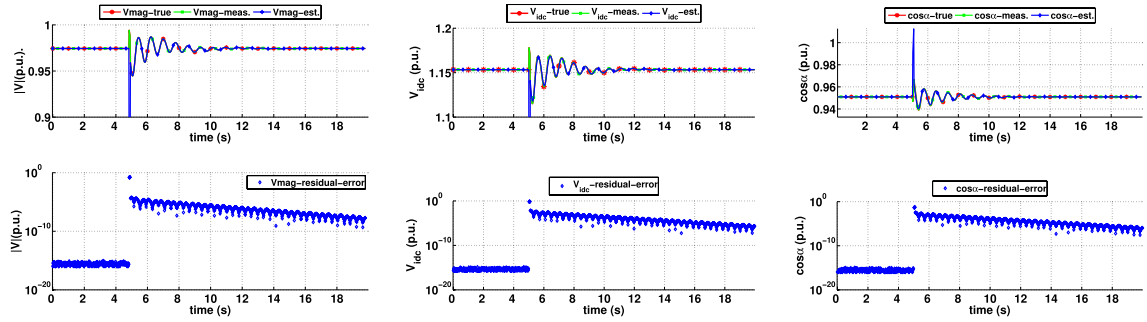

(a) Voltage magnitude at bus 4. (b) DC voltage at bus 4. (c) cos α.

Fig. 7. PSE for the six-bus hybrid AC/DC system for multiple snapshots.

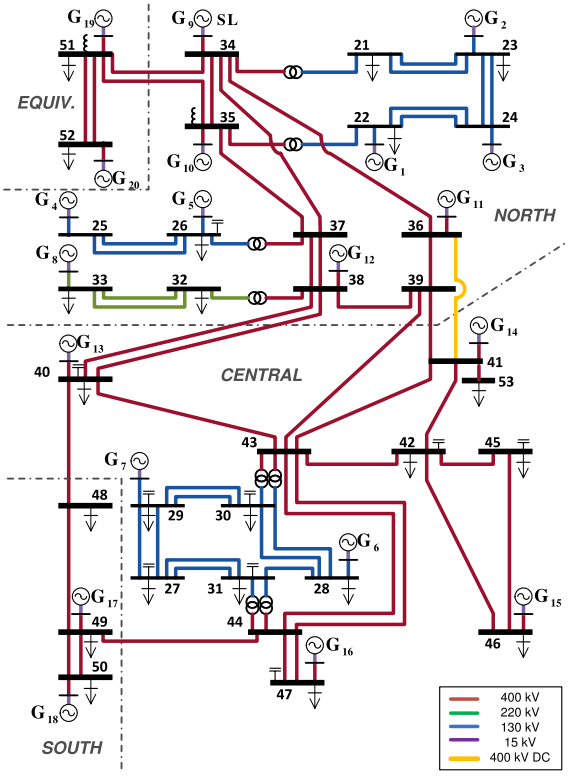

Fig. 8. The KTH-NORDIC32 hybrid AC/DC system.

HVDC link is added between bus 36 and bus 41, as shown by a yellow line in Fig. 8, for here onwards this model is referred to as the KTH-NORDIC32 hybrid AC/DC system [11].

A 0.4 p.u. (10%) load increase was applied at bus 41 at $t = 5$ s.

The state vector for the KTH-NORDIC32 hybrid AC/DC system is organized as follows

$$\mathbf{x} = [|\widetilde{V}_1|,\ |\widetilde{V}_2|\ \ldots\ |\widetilde{V}_{53}|,\ \theta_1,\ \theta_2,\ \ldots\ \theta_{53},\ |\widetilde{I}_1|,\ |\widetilde{I}_2|\ \ldots\ |\widetilde{I}_{160}|,\ \delta_1,\ \delta_2,\ \ldots\ \delta_{160}, |\widetilde{I}_r|,\ |\widetilde{I}_i|,\ \delta_r,\ \delta_i,\ V_{rdc},\ V_{idc},\ I_{dc},\ \cos\alpha,\ \cos\delta]^T.$$

The PSE procedure is the same as introduced in Section 6.1. As shown in Figs. 9 and 10, the PSE residuals remain as low as in Section 6.1, which indicates that the proposed PSE is not affected by the size of the test system. Fig. 10 validates that the proposed PSE algorithm is capable to estimate states even when the system is subject to a dynamic change (in this case, a sudden load change).

6.3. Simulation results for the scenario without DC measurements

The same test scenario as in Section 6.1 was applied here. To decrease the measurement redundancy, only the voltage phasor measurements at bus 3 and 4, and current phasor measurements on lines 3, 4, 7, and 8, which are incident to either bus 3 or 4, were provided. There was no DC state measurement provided and the estimation results are shown in Fig. 11.

Comparing Fig. 11 with the results in Section 6.1, reducing measurements redundancy does not significantly influence the PSE performance as long as the measurements can satisfy the observability requirements discussed in Section 5.1. This test scenario illustrates that when PMUs are available only at critical boundary buses between the AC system and the DC link, it is possible to estimate DC states without having any DC measurements.

6.4. Simulation results for the scenario with realistic measurement noises and corresponding weightings

The effect of measurement noises and weightings selection were studied using the same test scenario as in Section 6.1 by adding Gaussian white noise and using the weightings in Table 3. Fig. 12 shows the PSE computation results, in which the residuals are larger in comparison with the previous case in Section 6.1. Nevertheless, the state estimates are acceptable for the applied signal-to-noise ratios.

6.5. Simulation results for the scenario with angle bias correction

An example of angle bias correction was made for the six-bus hybrid AC/DC system, where a 7.5° angle jump at bus 1° and 30° angle jump on line 1, which is incident to the bus 1, were applied at $t = 10$ s and removed at $t = 11$ s as shown in Fig. 13. This test scenario shows that PSE also has the ability of correcting angle biases for hybrid AC/DC grids.[3]

6.6. Simulation time and computation performance

Referring to the estimation results in Sections 6.1 and 6.2, it is observed that most of the estimation errors are below 10^{-12} with relatively few iterations. PSE residuals that are higher than 10^{-12} are due to the lack of model update, and they require a larger number of iterations. For instance, in the test scenario of Section 6.1, the number of iterations for each estimation snapshot remained around 2 when the system was in steady state. During

[3] Note: measurements are shown in green; the solution from the PSE, is shown in blue.

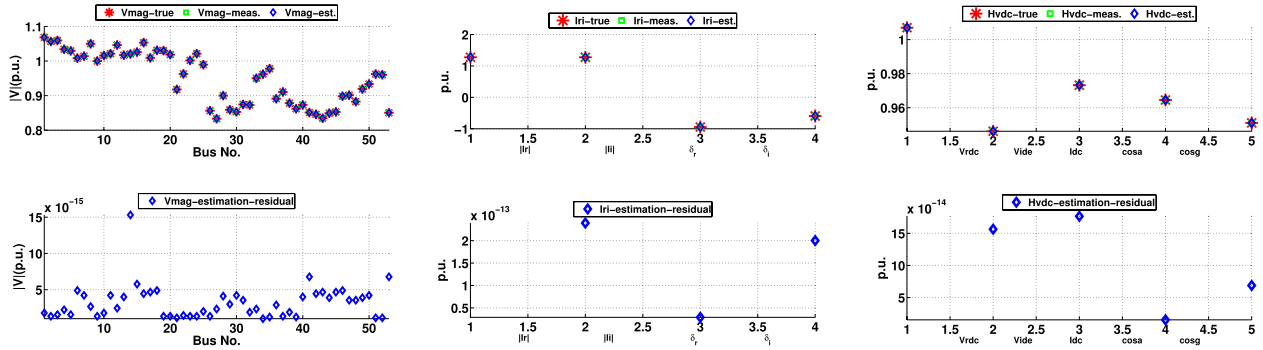

(a) Voltage magnitudes at all the buses for one snapshot.

(b) AC/DC interface states for one snapshot.

(c) DC states for one snapshot.

Fig. 9. PSE for the KTH-NORDIC32 hybrid AC/DC for a single snapshot.

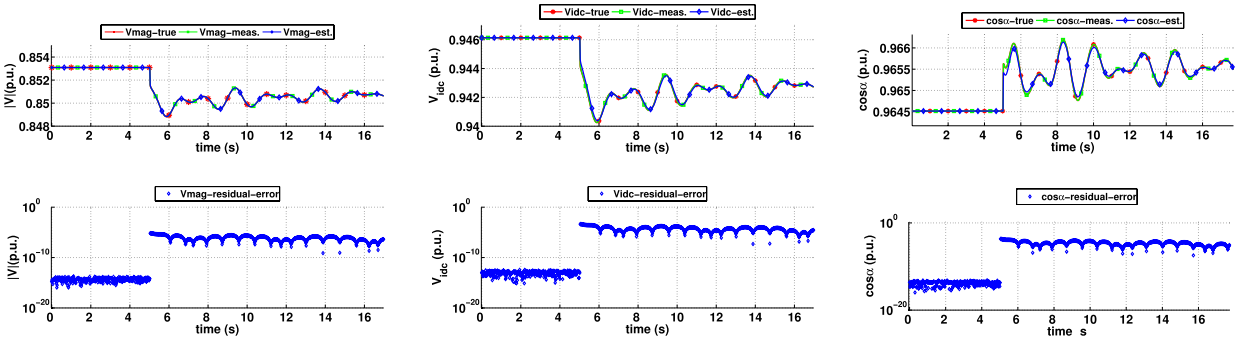

(a) Voltage magnitude at bus 41.

(b) DC Voltage at bus 41.

(c) $cos\alpha$.

Fig. 10. PSE for the KTH-NORDIC32 hybrid AC/DC system for multiple snapshots.

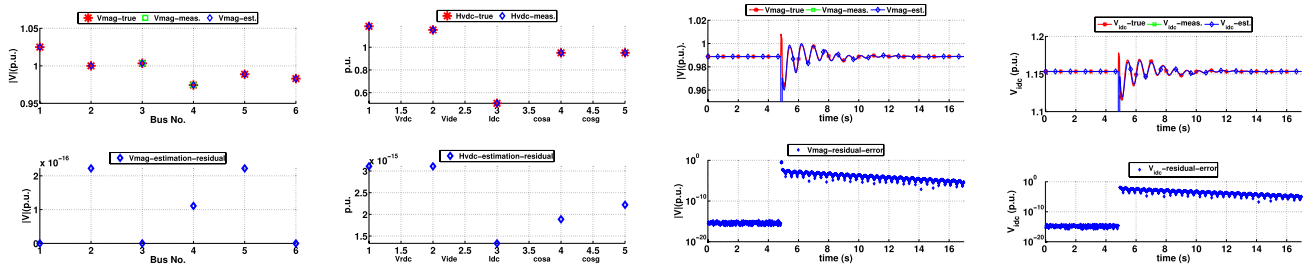

(a) Voltage magnitudes at all the buses for one snapshot.

(b) DC states for one snapshot.

(c) Voltage magnitude at bus 5.

(d) DC voltage at bus 4.

Fig. 11. Effect of reducing AC/DC measurements redundancy on the PSE for the six-bus hybrid AC/DC system.

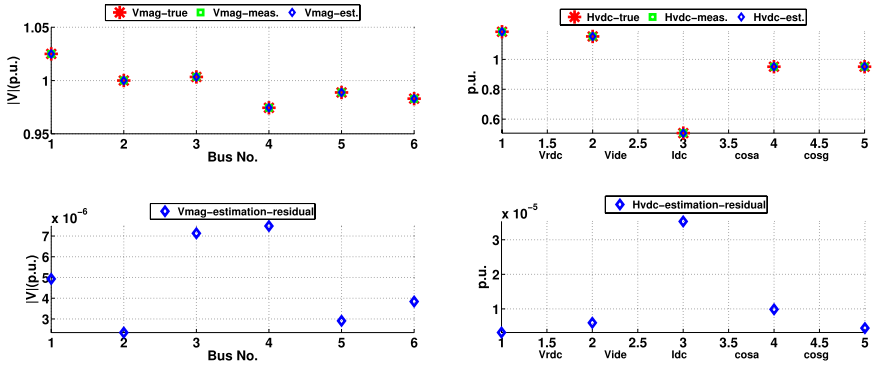

(a) Voltage magnitudes at all the AC buses at one snapshot.

(b) DC states at one snapshot.

Fig. 12. Effect of measurement noises on the PSE for the six-bus hybrid AC/DC system.

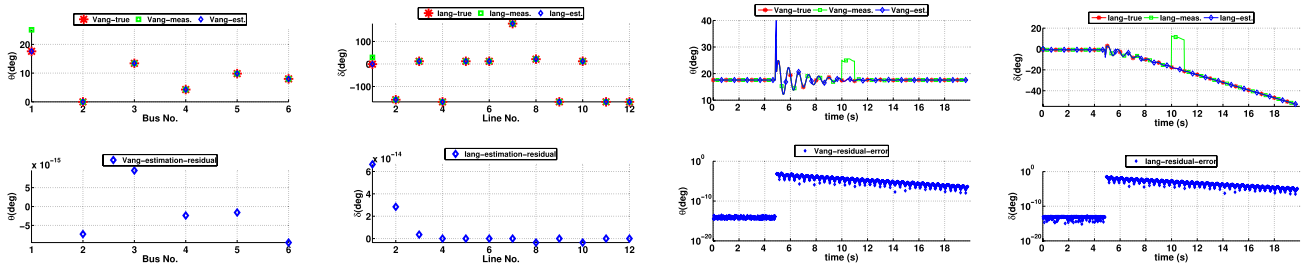

(a) Voltage angles for one snapshot (bus 2 is slack bus).
(b) Current angles on all the lines for one snapshot.
(c) Voltage angle at bus 1 (bus 2 is slack bus).
(d) Current angle on line 1 (between bus 1 and bus 3).

Fig. 13. Angle bias correction for the six-bus hybrid AC/DC system. (For interpretation of the references to colour in this figure legend, the reader is referred to the web version of this article.)

the first three cycles after the perturbation occurred, the iteration number was 37 at once, and then decreased to 4 after another three cycles. However, observe that this is due to the lack of model update.

PSE computation time statistics for the test scenario in Section 6.1 are shown in Table 4. Two hundreds and fifty out of 1000 measurement sets were obtained before the perturbation; the others were after the perturbation. The measurement sets for which the PSE computation time was below 0.003 s account for 23.7% of the whole measurement sets; more than 99.6% of the PSE computations are faster than the measurement rate, which is 0.02 s. Computation time exceeding the measurements interval mainly occurred during the perturbation period. This shows that the proposed PSE is fast enough to track system dynamics even when the network model is not fully updated. The time-performance of the algorithm in a standard PC (2.80 GHz Intel Core processor running MATLAB R2012b) is already acceptable for real-time applications with minimum delay, and could be improved if the code is optimized and re-implemented in a low-level programming language such as *C++*. In addition, it demonstrates the feasibility of implementing the PSE algorithm into real-time tests for future work.

Table 4
Statistics of the PSE computation time.

Computation time	No. of meas. sets (1000 in total)	%
$t \geq 0.02$ s	4	0.4%
$0.01 \leq t < 0.02$ s	5	0.5%
$0.006 \leq t < 0.01$ s	113	11.3%
$0.003 \leq t < 0.006$ s	641	64.1%
$t \leq 0.003$ s	237	23.7%

7. Discussion

Previous work in [11] presents a linear PSE, while the PSE proposed in this paper is a nonlinear one. The linearity (or nonlinearity) of a PSE algorithm refers to the applied numerical algorithm. A linear WLS algorithm or a nonlinear one is determined by the measurement error vector $\mathbf{e}(\mathbf{x})$. In most cases, this vector presents the same linearity (or nonlinearity) as the network model. The rationale to use the nonlinear PSE is explained below.

For the AC part, both algorithms use the same linear network model. However, since the state variables used in this paper are in polar coordinates, each linear equation needs to be rewritten into two equations associated with trigonometric functions of the phasor angles. These trigonometric functions introduce nonlinearities. Although this brings additional computational burden, using phasors in polar coordinates gives the significant advantage of allowing angle bias detection and correction, which has been addressed in Section 5.3.

To support this point, a comparison was performed on the same nine-bus AC test system as in [11] by using the linear and nonlinear PSE, respectively. A 7.5° angle bias was introduced to bus 8° and 30° angle biases to the lines that are connected with bus 8 for both cases.

Fig. 14 shows voltage magnitudes and angles' estimation results for the linear PSE when angle biases were introduced. The estimation accuracy for both magnitudes and angles reduces significantly compared to the results presented in [11] when no angle bias was introduced: magnitude residuals from 10^{-16} to 10^{-3}; angle residuals from 10^{-15} to 1. This indicates that the angle biases were not successfully detected; moreover, they contaminated other angles and even magnitudes being estimated. Therefore, it is verified that the linear PSE is unable to detect and

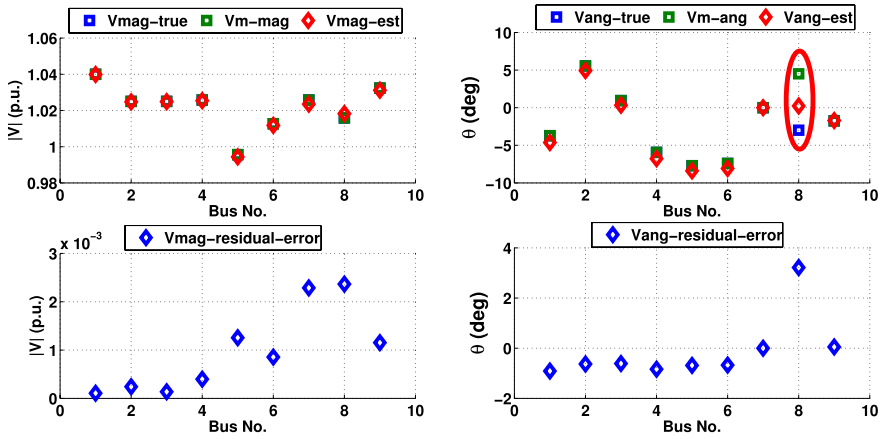

(a) Voltage magnitudes at all buses for one snapshot.
(b) Voltage angles at all buses for one snapshot.

Fig. 14. Linear SE results—voltage magnitudes and angles for a nine-bus test system when a 7.5° angle bias was introduced to bus 8.

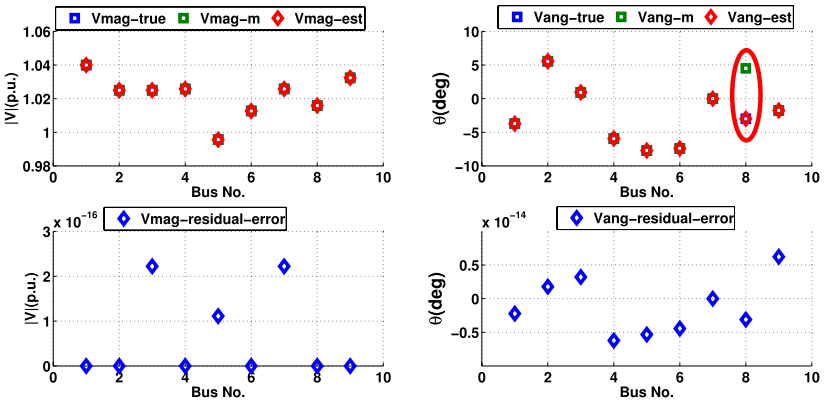

(a) Voltage magnitudes at all buses for one snapshot.

(b) Voltage angles at all buses for one snapshot.

Fig. 15. Nonlinear SE results—voltage magnitudes and angles for a nine-bus test system when a 7.5° angle bias was introduced to bus 8.

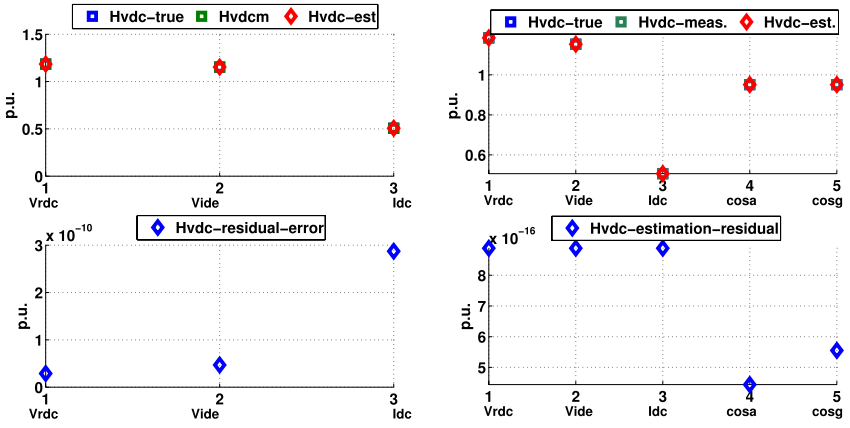

(a) DC states in linear PSE for one snapshot.

(b) DC states in nonlinear PSE for one snapshot.

Fig. 16. PSE results for the linear (left) and nonlinear (right) DC link models.

correct angle biases. Paper [40] also shows a simple example that draws the same conclusion.

On the contrary, the nonlinear PSE proposed in this paper successfully detected and corrected the angle bias. As shown in Fig. 15, estimation residuals remain the same range of accuracy as in the case when no angle bias is introduced.

The limitations of the linear SE approach was reported in [40], even in the case where there is full observability and redundant measurements (PMUs installed at all buses and measuring all the currents at each bus), the linear state estimator approach fails to provide the correct measurement residuals in the presence of an angle bias.

The DC network model can be simplified to a linear one as presented in paper [11] by reducing the number of equations and using complex variables. However, this will have two consequences: (i) the model loses valuable information on the HVDC link, and (ii) the state variables that must be used, for instance $|\widetilde{V}_r|\cos\alpha$, are not consistent with other variables, and this may lead to matrix conditioning issues during the linear least squares solution. Therefore, though the DC measurements are presumed to be very accurate, a more detailed classic HVDC link model is still preferred by the authors in order to guarantee estimation accuracy.

A comparison between the linear classic HVDC link model as in [11] and the nonlinear one was carried out and the results are shown in Fig. 16. Compared to the nonlinear model's estimation residual of 10^{-16}, the linear one only achieves 10^{-10}.

8. Conclusions and future work

A PMU-based state estimator for a hybrid AC/DC grid has been presented. By applying Kirchhoff's laws, the proposed network model simplifies the nonlinearities of the network model used in conventional SEs. All the AC and DC states are considered simultaneously to solve the nonlinear WLS problem. After posing the network model and measurement model for the PSE, computation results for two hybrid AC/DC grids are presented. Practical issues for applying this PSE algorithm in realistic conditions are briefly discussed, including system observability and measurement redundancy, measurement noises and weightings, angle bias, and computation performance.

In addition, this paper has highlighted the importance to perform quick updates to the system topology and network model. This calls the need for a PMU-based topology processing algorithm, for which, the work in [41] is a good starting point.

Future work will focus on developing a VSC-based DC link model, extending the DC link models to handle MTDC grids, and implementing the proposed PSE algorithm into a real-time platform to carry out end-to-end real-time hardware-in-the-loop performance tests [7].

Acknowledgments

W. Li is supported by SweGRIDS. L. Vanfretti is supported by Statnett SF, STandUP for Energy collaboration initiative,

STRONgrid, and iTesla. The economical support of these institutions is sincerely acknowledged.

References

[1] A. Monticelli, State Estimation in Electric Power Systems—A Generalized Approach, Kluwer Academic Publishers, Massachusetts, 1999.
[2] A. Abur, A.G. Expósito, Power System State Estimation: Theory and Implementation, Marcel Dekker, Inc., New York, 2004.
[3] A.G. Phadke, J.S. Thorp, K.J. Karimi, State estimation with phasor measurements, IEEE Trans. Power Syst. 1 (1) (1986) 233–238.
[4] L. Vanfretti, J.H. Chow, S. Sarawgi, B. Fardanesh, A phasor-data-based state estimator incorporating phase bias correction, IEEE Trans. Power Syst. 26 (1) (2011) 111–119.
[5] S.G. Ghiocel, J.H. Chow, et al., Phasor-measurement-based state estimation for synchrophasor data quality improvement and power transfer interface monitoring, IEEE Trans. Power Syst. 29 (2) (2014) 881–888.
[6] D. Shi, D.J. Tylavsky, N. Logic, An adaptive method for detection and correction of errors in pmu measurements, IEEE Trans. Smart Grid 3 (4) (2012) 1575–1583.
[7] L. Vanfretti, V.H. Aarstrand, M.S. Almas, V.S. Peric, J.O. Gjerde, A software development toolkit for real-time synchrophasor applications, in: IEEE PowerTech, June, 2013.
[8] M. Zhou, V.A. Centeno, J.S. Thorp, A.G. Phadke, An alternative for including phasor measurements in state estimators, IEEE Trans. Power Syst. 21 (4) (2006).
[9] A.S. Costa, A. Albuquerque, D. Bez, An estimation fusion method for including phasor measurements into power system real-time modeling, IEEE Trans. Power Syst. 28 (2) (2013).
[10] H. Sun, et al., Two-level state estimation method for power systems with SCADA and PMU measurements, in: ISGT Asia, May, 2012.
[11] W. Li, L. Vanfretti, Inclusion of classic HVDC links in a PMU-based state estimator, in: IEEE PES General Meeting, July, 2014.
[12] B. Xu, A. Abur, State estimation of systems with embedded FACTS devices, in: IEEE PowerTech, June, 2003.
[13] B. Xu, A. Abur, State estimation of systems with UPFCs using the interior point method, IEEE Trans. Power Syst. 19 (3) (2004) 1635–1641.
[14] P. Vaessen, A comparison of Smart Grid technologies: HVDC classic versus Voltage Source Converter HVDC [Online], 2013, Available FTP: http://smartgridsherpa.com/blog/a-comparison-of-smart-grid-technologies-hvdc-classic-versus-voltage-source-converter-hvdc.
[15] H.R. Sirisena, E.P.M. Brown, Inclusion of HVDC links in AC power-system state estimation, IEE Proc. Gener. Transm. Distrib. 128 (3) (1981) 147–154.
[16] Q. Ding, B. Zhang, T.S. Chung, State estimation for power systems embedded with FACTS devices and MTDC systems by a sequential solution approach, Electr. Power Syst. Res. 55 (3) (2000) 147–156.
[17] F. Milano, Power System Modeling and Scripting, Springer-Verlag, London, UK, 2010.
[18] P. Kundur, Power System Stability and Control, McGraw-hill, New York, 1994.
[19] A. Monticelli, F.F. Wu, Network observability: Identification of observable islands and measurement placement, IEEE Trans. Power Appl. Syst. PAS-104 (5) (1985) 1035–1041.
[20] B. Gou, A. Abur, A direct numerical method for observability analysis, IEEE Trans. Power Syst. 15 (2) (2000) 625–630.
[21] J. Chen, A. Abur, Placement of PMUs to enable bad data detection in state estimation, IEEE Trans. Power Syst. 21 (4) (2006) 1608–1615.
[22] T. Baldwin, L. Mili, M.B. Boisen Jr., R. Adapa, Power system observability with minimal phasor measurement placement, IEEE Trans. Power Syst. 8 (2) (1993) 707–715.
[23] B. Xu, A. Abur, Observability analysis and measurement placement for systems with PMUs, in: IEEE PES PSCE, Oct., 2004.
[24] R. Emami, A. Abur, Reliable placement of synchronized phasor measurements on network branches, in: IEEE PES PSCE, Mar., 2009.
[25] G. Krumpholz, K. Clements, P. Davis, Power system observability: A practical algorithm using network topology, IEEE Trans. Power Appl. Syst. PAS-99 (4) (1980) 1534–1542.
[26] T.L. Bladwin, et al., Power system observability with minimal phasor measurement placement, IEEE Trans. Power Syst. 8 (2) (1993) 707–715.
[27] D.J. Brueni, L.S. Heath, The PMU placement problem, SIAM J. Discrete Math. 19 (3) (2005) 744–761.
[28] D. Gyllstrom, E. Rosensweig, J. Kurose, On the impact of PMU placement on observability and cross-validation, in: ACM e-Energy, May, 2012.
[29] Guide to the expression of uncertainty in measurement, ISO-IEC-OIML-BIPM, 1992.
[30] S. Chakrabarti, E. Kyriakides, PMU measurement uncertainty considerations in WLS state estimation, IEEE Trans. Power Syst. 24 (2) (2009) 1062–1071.
[31] IEEE Guide for Synchronization, Calibration, Testing, and Installation of Phasor Measurement Units (PMUs) for Power System Protection and Control, in: IEEE Std C37.242-2013, Mar., 2013.
[32] Model 1133A Power Sentinel GPS-synchronized Power Quality Revenue Standard, Arbiter Systems, inc. Paso Robles, CA. Available: http://www.arbiter.com/files/product-attachments/1133a_manual.pdf.
[33] P. Yang, Z. Tan, A. Wiesel, A. Nehorai, Power system state estimation using PMUs with imperfect synchronization, IEEE Trans. Power Syst. 28 (4) (2013) 4162–4172.
[34] Q.F. Zhang, V.M. Venkatasubramanian, Synchrophasor time skew: Formulation, detection and correction, in: NAPS, Sep., 2014.
[35] N.G. Bretas, A geometrical view for multiple gross errors detection, identification, and correction in power system state estimation, IEEE Trans. Power Syst. 28 (3) (2013) 2128–2135.
[36] F. Milano, An open source power system analysis toolbox, IEEE Trans. Power Syst. 20 (3) (2005) 1199–1206.
[37] M.C. Stubbe, Long Term Dynamics Phase II Final Report, Cigre, Tech. Rep. Task Force 38.08.08, March, 1995.
[38] T. Van Cutsem, Description, Modelling and Simulation Results of a Test System for Voltage Stability Analysis, IEEE Working Group on Test Systems for Voltage Stability Analysis, Tech. Rep. Version 1, July, 2010.
[39] Y. Chompoobutrgool, Development and implementation of a nordic grid model for power system small-signal and transient stability studies in a free and open source software, in: IEEE PES General Meeting, July, 2012.
[40] L. Vanfretti, J.H. Chow, Synchrophasor data applications for wide-area systems, in: PSCC, Aug., 2011.
[41] M. Farrokhabadi, L. Vanfretti, An efficient automated topology processor for state estimation of power transmission networks, Electr. Power Syst. Res. 106 (2014) 188–202.